

# In situ small-scale hydrogen embrittlement testing made easy: An electrolyte for preserving surface integrity at nano-scale during hydrogen charging

Tarlan Hajilou<sup>a,\*</sup>, Malin.S.B. Hope<sup>a</sup>, Amin Zavieh<sup>a</sup>, Nousha Kheradmand<sup>a</sup>, Roy Johnsen<sup>a</sup>, Afrooz Barnoush<sup>a,\*\*</sup>

<sup>a</sup>*Department of Mechanical and Industrial Engineering, NTNU, Richard Birkelands vei 2b,7491 Trondheim, Norway*

---

## Abstract

An electrolyte for electrochemical hydrogen charging of corrosion-susceptible alloys is developed, which preserves the surface integrity at nano-scale by minimizing the surface roughness alternation. To assure the formation and adsorption of the hydrogen from the electrolyte, permeation tests were performed on Fe 3wt.%Si ferritic steel. X-ray photoelectron spectroscopy method was used to check the effect of the glycerol-based solution on the chemical composition of the sample surface. The surface analysis revealed minimal chemical and topography alteration on the surface after different electrochemical treatments. Various types of in situ small-scale mechanical tests such as nano-indentation, micro-pillar compression, and micro-cantilever bending tests were performed inside this electrolyte while the samples being charged with hydrogen under cathodic potential. These small-scale mechanical tests showed that the solution facilitates studying hydrogen embrittlement in nano- or micro-scale.

*Keywords:* hydrogen-assisted cracking, electrochemistry, hydrogen diffusion, nano-indentation, micromechanical

---

## 1. Introduction

Most high strength and high performance alloys will experience a premature rupture when exposed to hydrogen (H) [1, 2]. This phenomenon is called hydrogen embrittlement (HE) which is caused by the presence of H in metals [3]. H typically gets into the metal by surface adsorption followed by absorption and the diffusion/trapping phenomenon [4]. A vast amount of scientific research has been carried out on HE since 1874 when the very first report about the deleterious effect of H on the mechanical properties of steel was published by Johnson [5]. These researches led to several proposed mechanisms [6–11]. Interaction of the H with microstructure and crystal defects, such as dislocations, vacancies, phase boundaries, grain boundaries, or precipitates (e.g. carbides) is determinant factor toward understanding the HE phenomenon [12–15]. In a typical macroscopic test, these defects that are distributed within the sample will start to interact with H at different incidents within the course of the testing [16–18]. Due to the large scale of the test and the large number of the defects involved, it is very hard to get mechanistic insight from the interaction of the defects with H. Such a mechanistic knowledge of H effect on defects is extremely valuable for

---

\*Corresponding author

\*\*Corresponding author

*Email addresses:* tarlan.hajilou@ntnu.no (Tarlan Hajilou), afrooz.barnoush@ntnu.no (Afrooz Barnoush)

modeling the HE phenomena and development of predictive tools which are highly demanded by the industry. One possible approach to study the mechanism of the H interaction with different microstructural features in detail and gain mechanistic information is to perform micromechanical [19–21] or nanomechanical [22–24] tests. Investigation of HE phenomenon in small scales imposes some experimental complications. As an example, in situ H charging is mandatory versus ex situ H charging for most metals [25, 26]. Because, out gassing of H from small-scale samples leads to the rapid H out-gassing and depletion. The necessity of in situ testing becomes more pronounced for the alloys with higher H diffusion rate [27]. Electrochemical charging of H is one of the extensively utilized approaches in the literature [28, 29]. However, a major challenge during small-scale testing combined with electrochemical charging of the sample is to preserve the surface roughness and the integrity of the micron-sized samples at the nanometer scale. Usually, in situ electrochemical small-scale testing takes several hours (including charging and testing time under slow strain rates) to accomplish. As a result, preserving integrity of the nano- or micro-scale samples turns to a challenging issue. Post-mortem analysis such as electron backscatter diffraction (EBSD) or electron channeling contrast imaging (ECCI) of the in situ electrochemically H charged and tested surface or micron-sized samples also requires an intact surface quality [30, 31]. Under cathodic electrochemical potentials, although the overall surface would be preserved from corrosion, local variations in electrochemical potentials and chemistry of the electrolyte such as dissolved oxygen content and pH will result in small local areas corrosion and alteration of the surface which is unacceptable for small-scale testing while in a macroscopic test can be easily disregarded. The authors experienced the destruction of the small-scale testing samples (1 micrometer in diameter pillars) inside the borate buffer solution which is known to be a non-corrosive solution for iron base alloys [32]. These pillars were under cathodic polarization for several hours (Fig. 1). Experienced failure was the motivation for developing the solution introduced in this paper.

[Figure 1 about here.]

To overcome this problem, we used a similar strategy as proposed by Macák et.al [33, 34]. They increased the viscosity of the electrolyte by replacing water with glycerol to control local concentration fluctuations and pH bursts in the electrolyte for growing nanotubes longer than 500 nm with higher aspect ratio inside acidic based solutions. Here, we report the application of such glycerol-based electrolyte for H charging during in situ small-scale mechanical testing to assure the sample surface integrity in nanometer scale. To show the applicability of this new electrolyte as a medium for electrochemical H charging, we performed electrochemical H permeation tests to confirm the H generation and uptake on the surface and to estimate subsurface H concentration (Section 3.2). Further, the sample surface composition was analyzed using the X-ray photoelectron spectroscopy (XPS) method after electrochemical charging under both cathodic and anodic current densities and the results were compared to the electropolished sample (Section 3.3). XPS analyses were carried out in order to investigate the probable effect of the new solution on the surface chemical composition during electrochemical charging. Several types of in situ small-scale testing such as in situ electrochemical nano-indentation, in situ electrochemical micro-pillar compression, and in situ electrochemical cantilever bending tests were successfully performed inside the glycerol-based solution to show the capability of using

this electrolyte in the small-scale testing of steels (Section 3.4).

## 2. Experimental procedure

### 2.1. Material

50 Sodium Tetraborate, Decahydrate, ACS Grade with a 99.5% purity ( $\text{Na}_2\text{B}_4\text{O}_7 \cdot 10\text{H}_2\text{O}$ ) from VWR chemical company and glycerol anhydrous for synthesis  $(\text{HOCH}_2)_2\text{CHOH}$  from Merck company with a purity higher than 99% were used to make the electrolyte. The composition of the solution was 1.3 mol/L borax in glycerol and diluted with double distilled water of 20 volume percent to obtain the adequate conductivity. A Consort K911<sup>®</sup> instrument was used for resistivity measurements. The solution had a resistivity of 380  $\Omega\text{cm}$  at 25 °C. This number decreased to  
55 290 and 160  $\Omega\text{cm}$  at 30 and 50 °C, respectively. A PHM210 Standard pH Meter<sup>®</sup> was used for pH measurement. The pH of this solution was  $\sim 7$  and the boiling point was measured to be  $\sim 106$  °C. Differential scanning calorimetry (DSC) technique was used to measure the freezing point of the solution. DSC 250<sup>®</sup> from TA Instruments was used to perform the test. According to the heat flow- temperature curve presented in Fig. 2, there is a distinct change in the heat flow slope around  $\sim -58$  °C which is considered as the start point for the freezing peak. The reported curve was  
60 obtained at 10 °C/min scan rate measurements from 40 °C to  $-80$  °C. Since decreasing the cooling rate gives a narrower and sharper freezing peak [35], no detectable change was seen in the DSC measured thermogram by 2 °C/min cooling rate down to  $-80$  °C.

[Figure 2 about here.]

Fe-3wt.%Si alloy, which is a simple ferritic steel, was chosen as the testing material in this study. The chemical  
65 composition of the alloy is provided in Table 1.

[Table 1 about here.]

This material has a high diffusivity and low solubility for H that is typical for ferritic steels [6, 36]. Fe-3wt.% Si, similar to other low alloy steels, has low corrosion resistance [37] and widely used in HE studies [8, 38]. The alloy was received in coil form with 1 mm thickness. Disc-shaped samples were cut from the coil by electrical discharge  
70 machining in diameters of 12 mm and 29 mm for in situ mechanical and permeation testing, respectively. The samples for in situ mechanical test were heat treated at 1200 °C under vacuum at a base pressure of 1 mPa for one week and cooled in furnace to achieve coarse grains in the range of millimeters.

### 2.2. Permeation test

#### 2.2.1. Apparatus and sample

75 A permeation cell made from glass with a capability of sealing all the openings was used in this study. This enables submerging the permeation cell into a water bath of steady temperature. The testing sample was located between the

two cathodic and anodic cells, and sealed using a part made out of Kel-F<sup>®</sup> (Polychlorotrifluoroethylene) and POM (Polyoxymethylene). Platinum wires and silicon gaskets were used as the counter electrode and sealing for the caps, respectively. Hg/HgSO<sub>4</sub> type reference electrode was used during the tests and all the potentials were reported versus this reference electrode. The permeation cell was submerged into a water bath. The complete permeation setup including the water bath was placed inside a Faraday cage. The diameter and the thickness of the sample were 29 mm and 0.95 mm, respectively. The sample surface was prepared by grinding down to grit No. 4000 and mechanical polishing down to 1 μm on both cathodic and anodic sides. The exposed area of the sample was 4.4 cm<sup>2</sup> after mounting between the compartments of the cell.

### 2.2.2. Testing procedure

Two GAMRY reference 600+ potentiostats were used to control the current and the potential under galvanostatic and potentiostatic modes in the cathodic and anodic cells, respectively. Open circuit potential (OCP) measurements were done on each side of the cell for ~ 2 hours, up to reaching a steady state potential. The OCP potential was measured to be ~ -1100 mV on each permeation side. A potentiostatic potential of 0 mV was applied in the anodic compartments for 24 hours so that we could extract all of the possible diffusible H present in the sample. After reaching a steady state value, the current is considered as the background current. Galvanostatic charging was used in the cathodic side. Permeation tests were performed under -100, -50 and -10 μA/cm<sup>2</sup> cathodic current densities while keeping the bath temperature constant at 50 °C. One additional test with a cathodic current of -10 μA/cm<sup>2</sup> at 30 °C was also done to check for H permeation inside the new electrolyte, at low current density and temperature. During charging transient, the current in the cathodic side was kept constant until a steady state value had been reached on the anodic side. Single anodic polarization was used during discharging transients. Current measurements in the anodic side continued until a new steady state had been reached when all of the diffusible H in the sample was diffused out. During the charging and discharging transients, the anodic potential was kept constant at 0 mV. Three sets of charging and discharging transients were repeated in each permeation test condition. One sample was used during the main and additional series of the permeation tests without stopping the tests. The presence of irreversible trapping sites was only possible to be evaluated by comparing the data from the first and subsequent H charging transients under the testing condition of -100 μA/cm<sup>2</sup> and 50 °C. Irreversible trap sites are usually defined as microstructural sites at which H has long residence time and larger binding energy relative to migration energy for diffusion [39]. All this type of trapping sites is occupied during the first permeation transient done on the sample. The difference between the first and subsequent permeation transient can be used to evaluate the presence of irreversible trapping site in the sample.

### 2.3. Electrochemical testing

The used electrochemical cell was a three-electrode setup, consisted of sample as the working-, platinum wire as the counter- and Hg/HgSO<sub>4</sub> reference electrodes. Reference electrode was connected to the cell through a double

110 junction. The same cell was used for in situ small-scale mechanical testing in combination with the nano-indentation setup. All potentials in this work were reported versus Hg/HgSO<sub>4</sub> reference electrode. The polarization curve of the Fe-3wt.%Si alloy was obtained at room temperature with a scan rate of 1 mV/s after being kept at OCP for 10 min, in the glycerol-borax solution using a PGU-1A-OEM<sup>®</sup> instrument from IPS company.

#### 2.4. X-ray photoelectron spectroscopy

115 The XPS method was used to check the effect of the glycerol-based solution on the chemical composition of the sample surface under both cathodic and passive currents. Fe-3wt.%Si samples with three different charging backgrounds were compared with one another. The first sample was electropolished using a mixture of methanol and sulfuric acid after grinding and mechanical polishing [40]. After electropolishing, the root mean square (RMS) surface roughness was 1.5 nm. This sample will be called “EP” in the text. The second sample was electropolished and kept at OCP potential for 10 min and charged under cathodic potential of -1400 mV for 5 hours. The second sample will be called “EP+C” in the text. The third sample was electropolished and then kept at OCP potential, -1400 mV cathodic potential and 0 mV anodic potential for 10 min, 5 hours and half an hour, respectively. This sample will be called “EP+C+A” in the text. The samples were rinsed with splash of distilled water and ethanol to remove the excess electrolyte to avoid further reactions on the surface. Then the samples were transferred straight to the XPS analysis inside a desiccator to minimize the time and any interference from the environment. The XPS analysis was carried out using a Kratos Axis Ultra DLD<sup>®</sup>. A monochromatic Al K $\alpha$  source (15 mA, 12 kV) was used for spectrometry. The sample analysis chamber pressure was  $1 \times 10^{-9}$  Torr (0.13  $\mu$ Pa) during the operation. Elemental maps were collected with pass energy of 160 eV with two sweeps. High resolution regional acquisitions were performed with pass energy of 20 eV with three sweeps and 0.1 eV step size for each element. Argon sputtering was performed by an ion gun in the analysis chamber, with an argon pressure of  $3.8 \times 10^{-6}$  Torr and an energy of 4 kV. Ar2p<sub>3/2</sub> at 241.1 was used to calibrate the binding energies. The analysis area was  $300 \times 700 \mu\text{m}^2$ . Using Casa XPS software, regional peaks were analyzed and fitted by Shirley background subtraction [41]. For curve fitting, evaluation and quantification, Gaussian/Lorentzian asymmetry was used and full width half maximum (FWHM) was kept constant for oxide components. The XPS spectra were analyzed for Fe2p<sub>3/2</sub>, O1s, Si2s and C1s elements [42, 43].  
135 The peak parameters of different observed compounds are listed in Table 2.

Surface analysis was done on the surface after electrochemical tests and after surface sputtering sequences of 10 , +60, +160, +260, +360, +860, +1360 and +2360 s for all the three samples.

[Table 2 about here.]

#### 2.5. In situ small-scale testing

##### 140 2.5.1. In situ electrochemical nano-indentation

An in situ electrochemical nano-indentation test was performed using a Hysitron TI950 TriboIndenter<sup>®</sup> system with an integrated miniaturized electrochemical cell, as described in Section 2.3. Detailed information about the

electrochemical cell integrated into the nano-indenter device can be found in [40]. The Fe–3wt.%Si sample surface used for in situ electrochemical nano-indentation was prepared by grinding down to grit No. 4000. The sample was electropolished for 30 seconds in a mixture of methanol and sulfuric acid afterwards.

The in situ nano-indentation test was done after 1 hour of cathodic charging at –1400 mV and 10 min after switching to anodic potential of 0 mV on the same sample. The in situ indentation results were compared with the indents done on the electro polished surface in air before starting the in situ electrochemical testing. The indenter tip used for the nano-indentation was a Berkovich diamond tip, which was specially designed for testing in liquid. The load function used for the load– controlled indentation consisted of a loading segment with a 12.5 mN/s loading rate and a 0.5 s holding time at the peak value of 2000  $\mu$ N. The unloading rate was 12.5 mN/s. For all three samples, the surface was imaged using the scanning probe microscopic imaging option that is provided by Hysitron TI 950 TriboIndenter<sup>®</sup> before and during charging.

### 2.5.2. *In situ electrochemical pillar compression and cantilever bending test*

Micro-pillar compression and micro-cantilever bending tests were performed inside the glycerol-based solution. A schematic drawing of the in situ electrochemical small-scale testing setup is shown in Fig. 3.

[Figure 3 about here.]

Single crystalline pillars with  $(\bar{5} 1 3)$  surface normal direction and average diameter of 1  $\mu$ m and micro-cantilevers with pentagonal cross-sections with  $(1 0 1)$  surface normal were cut using a FEI Helios Dual Beam<sup>™</sup> FIB system, with an acceleration voltage of 30 kV. In addition, a notch was milled along the  $(0 1 0)$  plane in  $[1 0 1]$  direction on the cantilevers. The diameter and depth of the notch were  $\sim 30$  nm and  $\sim 300$  nm, respectively. Fig. 4 shows the representative scanning electron microscopy (SEM) images of a micro-pillar and cantilever before testing. The micro-pillars and cantilevers were deformed under displacement control mode with a displacement rate of 1 and 2 nm/s, respectively. Long shaft flat punch and conical diamond tips were used during the in situ compression and bending tests, respectively. At least three samples were tested under air (EP) and cathodic H charging at –1400 mV (EP+C) conditions. More detailed information about the testing procedure can be found elsewhere [44, 45].

[Figure 4 about here.]

## 3. Results and discussion

### 3.1. *Polarization curve*

The polarization curve of the Fe–3wt.%Si sample is shown in Fig. 5. The polarization was performed between –2000 mV and 1500 mV from cathodic to anodic direction. The sample was in the cathodic branch up to  $\sim -1100$  mV and passed the active dissolution region from  $\sim -1100$  mV up to  $\sim -500$  mV. The passive region was between –500 and 500 mV. The current again began to increase with further anodic polarization, presumably because of the

onset of oxygen evolution. The values obtained from the polarization curve in this study are similar to the published  
 175 results obtained from the cathodic to anodic polarization of iron in aqueous borate-buffer solution with pH of 8.4 [46].  
 The small differences in the potentials and the current values can be caused by the limited difference in the sample  
 chemical composition, the electrolyte viscosity and conductivity which is caused by replacing water with glycerol  
 in this study. The two potential levels–1400 mV (cathodic) and 0 mV (anodic) were selected from the polarization  
 curve, for in situ electrochemical nano-indentation tests and surface chemical composition characterization.

180 [Figure 5 about here.]

### 3.2. Permeation test

Fig. 6 shows the permeation transient of the Fe–3wt.%Si for three charging current densities of –100, –50 and  
 –10  $\mu\text{A}/\text{cm}^2$  at 50 °C and for –10  $\mu\text{A}/\text{cm}^2$  at 30 °C plotted as steady-state normalized permeation flux (J) vs. the  
 logarithm of normalized time. The three tested charging transients are shown for each testing condition. The ideal lat-  
 185 tice diffusion calculated for the iron (BCC) by the Fick’s second law is also plotted for comparison. Overlapping or the  
 small shift between the permeation transients approved the repeatability of the permeation tests results. In addition,  
 since the first permeation transient was started at 50 °C and –100  $\mu\text{A}/\text{cm}^2$  condition, the overlapping of the perme-  
 ation curves suggested the absence of irreversible trap types in the tested material. According to the ASTM G148-97,  
 H permeation standard practice, the presence of irreversible trapping sites steeps the first permeation transient curve  
 190 and shifts it to the delayed time, which was not observed for the tested sample.

[Figure 6 about here.]

The effective diffusion coefficient ( $D_{\text{eff}}$ ) and subsurface H concentration ( $C_0$ ) obtained from permeation tests are  
 summarized in Table 3. The reported  $C_0$  was calculated using Eq. 1.

$$C_0 = \frac{i_{\text{ss}}L}{FD_{\text{eff}}} \quad (1)$$

where  $i_{\text{ss}}$  is the atomic H permeation current at steady state,  $L$  is the specimen thickness, and  $F$  is the Faraday constant.  
 $D_{\text{eff}}$  is calculated according to  $D_{\text{eff}} = L^2/6t_{\text{lag}}$ , with  $t_{\text{lag}}$  as the time to achieve a value of  $i(t)/i_{\text{ss}} = 0.63$ .

Decreasing the current density and testing temperature to –10  $\mu\text{A}/\text{cm}^2$  and 30 °C delayed the the saturation time  
 195 to the average  $t_{\text{lag}}$  of 6500 s which was around twice the time comparing to the  $t_{\text{lag}}$  achieved for the tests done at  
 50 °C. Pérez Escobar et al. reported that the saturation time and subsurface H concentration depend on the charging  
 conditions, such as the used electrolyte, the testing temperature, charging current, sample geometry and the type  
 of alloy [47]. Although the saturation time was delayed by lowering the testing temperature and current density,  
 oxidation current density was detected in the anodic side of the cell. This assured the H adsorption and diffusion  
 200 through the tested ferritic steel sample using the glycerol-borax solution.

Before the permeation tests, the sample surfaces on both sides were polished down to 1  $\mu\text{m}$  which helped for  
 higher subsurface H concentration during electrochemical charging. Hydrogen recombination ( $\text{H}_2$ ) increases as the

sample surface roughness increases and this lowers the amount of atomic H which can enter the metal [47, 48]. On the other hand, the actual current density increases as roughness decreases and this means that the sample can be charged more quickly [49]. Using an aqueous based solution, a palladium coating is used in some studies to prevent corrosion on the anodic side of the sample during the permeation tests [50]. However, in this study using the glycerol-based solution the anodic side of the sample was kept uncoated. Passive oxide layer thickness was investigated by XPS and will be discussed more in section 3.3.

[Table 3 about here.]

The  $D_{\text{eff}}$  values reported in Table 3 are approximately one to two order of magnitude smaller in comparison to the values reported earlier as lattice H diffusion coefficient for pure iron [51]. There can be several reasons for the obtained smaller  $D_{\text{eff}}$  in this study. For example,  $D_{\text{eff}}$  measurement during complete H charging and discharging transients involves reversible traps, which is supposed to be lower than the lattice diffusion coefficient [52]. Another reason can be the presence of the 3wt% Si in the chemical composition of the alloy that is used, which influences and decreases the  $D_{\text{eff}}$  value[53]. Additionally, the calculation of  $D_{\text{eff}}$  based on  $t_{\text{lag}}$  method is based on the assumption that diffusion is the rate controlling step in the whole process of the permeation. This assumption can be wrong in combination with the glycerol-based electrolyte for our setup, which is designed based on the ASTM G148-97 for permeation test in aqueous solution. However, our main intention from the permeation test was not to measure the exact H diffusion coefficient but to get assured about the H uptake and adsorption by charging the sample under cathodic potential inside the new electrolyte. In addition to this assurance, the probability of sample surface chemical composition alternation under cathodic or anodic currents were also needed to be checked, which will be discussed in the next section.

### 3.3. Surface analysis

The XPS method was used to further analyze the chemical composition of the sample surface in three different testing conditions. Fig. 7 compares the atomic concentration of Fe, O, C and Si elements versus the sum of sputtering time at three testing conditions. All the three samples had a very similar composition on the surface (not sputtered surface). Same kind of oxide film formation was due to inevitable air contact of the sample during splash rinsing and transferring of sample from desiccator to XPS chamber. However, after 70 s surface sputtering, EP+C and EP+C+A samples had higher oxide concentration compared to the EP sample. Despite the high oxide content at the surface of EP+C+A sample, by increasing the sputtering time the oxide content drops with a larger slope. In other words, the oxide content is higher for EP+C+A at the surface, but the oxide layer is thinner.

All three samples had relatively similar chemical composition after 500 s sputtering, as shown in Fig. 7. Comparing the percentage of different iron components in Fig. 8 for the three samples, all of the oxide components follow the same trend of decrease or increase in spite of small differences in their percentage.



235 There was more  $\text{Fe}_3\text{O}_4$  oxide than the other oxide components at a very close distance to the surface. The dominant  
oxide was FeO in all of the samples (above 80 %) after 10 second surface sputtering. The percentages of  $\text{Fe}^{3+}$  and  
 $\text{Fe}_3\text{O}_4$ , which were supposed to be higher near to the surface, decreased quickly as the sputtering time increased.  
There is possibility for  $\text{Fe}^{3+}$  to reduce to  $\text{Fe}^{2+}$  when the surface is sputtered by argon ion [42]. However, in the three  
240 tested samples there was a considerably large percentage of  $\text{Fe}_3\text{O}_4$  (~ 30 to 40 %) and  $\text{Fe}^{3+}$  (~ 10 %) after a long  
sputtering time. In the case of little reduction, it is considered to be the same for all of the samples due to similarity  
in the nature of the components and elements in all the samples.

Comparing the time where the atomic % Fe and O intersects each other in Fig. 7, all three samples have a relatively  
close intersection time. Comparing the decreasing slope of O and increase of Fe elemental peak area, it can be  
concluded the EP+C+A sample has a thinner and more concentrated oxide layer compared to the other samples.  
245 The EP+C+A sample reaches 50 % maximum oxide concentration earlier, where it is considered as the bulk [54].  
The active dissolution of the passive layer inside borate-buffer solution with a pH lower than 7 was investigated by  
Schmidt and Strehblow. They reported the thickness of the passive layer cannot exceed ~ 2 – 3 nm due to active  
dissolution [42]. In addition, Madiano et al. reported that passive film reduction happens during H diffusion, which  
may be is another reason for the thinner observed oxide layer under passive current density [55]. Fig. 9 compares  
250 the atomic ratio of O/Fe elements in the three testing samples. The EP+C+A sample has the highest O/Fe ratio at  
the surface; however, upon increasing the sputtering time, all of the samples showed a relatively similar O/Fe ratio.  
The O/Fe ratio comparison also confirms the enhanced dissolution of the passive layer in the EP+C+C sample. The  
iron XPS peaks with the fitted components are compared for the three testing samples after 230 and 3000 s sputtering  
time in Fig. 10. The  $\text{Fe}2p_{3/2}$  peak for EP sample showed a higher area compared to the other samples after 230 s.  
255 After 3000 s sputtering time, (when the oxygen element peak area is under its half amount for all three samples) the  
EP+C+A sample had a larger amount of  $\text{Fe}2p_{3/2}$ . XPS calculations suggested that using the new electrolyte during  
cathodic and anodic electrochemical testing does not cause a recognizable alternation to the sample surface chemical  
composition in comparison to the EP condition. Through permeation and XPS sections the possibility of charging the  
sample with H without any alternation in the surface chemical composition is discussed. The last verification step of  
260 the glycerol-based solution for the small-scale H charging was in situ electrochemical small-scale testing, is presented  
in the next section.

[Figure 7 about here.]

[Figure 8 about here.]

[Figure 9 about here.]

265 [Figure 10 about here.]

### 3.4. In situ small-scale testing

#### 3.4.1. In situ electrochemical nano-indentation

Fig. 11 shows the load-displacement (L-D) curves for the nano-indentation tests done under in situ cathodic and anodic electrochemical testing conditions and compared with the nano-indentation tests done on the EP sample in air. The instability area in the L-D curve, transition area from elastic to plastic deformation, is called pop-in, which is related to dislocation nucleation beneath the indenter during indentation [56]. There is an obvious change in the pop-in load and width of the sample when the electrochemical current is switched to cathodic and indentations done under H charging condition. In contrast to cathodic condition, switching to anodic potential brought the pop-in load and width to a comparable pop-in load and width obtained for the EP sample. The pop-in load and width decrease under cathodic current can be explained through the H enhanced dislocation nucleation [22]. This is approved by defectant theory. According to the theory, defect formation energy—that is, dislocation nucleation energy—will be lowered in the case of H segregation to defects [11]. These results are in agreement with previous works done by Barnoush et al. on FeAl, Al, Cu and Ni sample inside the aqueous solutions [57, 58]. For the case of low alloy steels, such as Fe-3wt.% Si, switching to anodic currents had been a problem due to increase in the sample's surface roughness. For the sake of precision, before using the glycerol-based solution, the pop-in results in air and under cathodic charging were compared because keeping the sample surface integrity at nano-scale at constant condition is a key factor for small-scale testing [40]. However, the new electrolyte provides the possibility of switching to passive currents during in situ nano-indentation tests still preserving the surface roughness in nano-scale.

Fig. 11 shows the scanning probe microscopy images of the three testing samples. The surface root mean square roughness was compared for the three samples in 100  $\mu\text{m}^2$  imaged area and it was 1.5, 2.1 and 1.8 nm for EP, EP+C and EP+C+A samples, respectively. By combining these data with sample surface composition data in Section 3.3, it can be concluded that the pop-in load changes observed during in situ electrochemical nano-indentation tests were related to H absorbed to the subsurface during cathodic charging of the sample, irrespective of the sample surface roughness or surface composition changes during electrochemical processes. According to the in situ nano-indentation test results, the pop-in load and width decreased under cathodic current comparing with EP sample, while the XPS results show similar composition and oxide decreasing trend in these two samples. Switching to anodic potential and extracting the subsurface H out of the sample, pop-in load increases again to a comparable condition to the EP sample. While there was a small difference in the surface oxide thickness of the EP+C+A sample comparing the EP sample, the pop-in load and width were in a comparable range. Therefore, the observed decrease in the pop-in load under cathodic charging condition is related to the presence of subsurface H. The in situ nano-indentation results and sample roughness analyses shows the usefulness of the glycerol-based solution for small-scale testing under both cathodic and anodic electrochemical current densities by preserving the surface integrity at nano-scale.

[Figure 11 about here.]

### 3.4.2. *In situ electrochemical pillar compression*

300 Any small changes in the sample surface condition during in situ electrochemical charging, such as localized corrosion or surface roughness change, can affect the dimensional integrity of the micron-sized testing samples. To study the H effect on the mechanical behavior of the materials, in situ compression tests were done by Barnoush et al. on Ni and FeAl pillars [44]. However, in situ pillar compression tests were not successful for pure iron and low alloy steels due to surface roughness alternation inside aqueous borate buffer solution with pH of 6.2. (Fig. 1).

305 A glycerol-based solution was used as an alternative for in situ pillar compression test on Fe-3wt.% Si alloy. Fig. 12 shows the SEM images of the pillars with 1  $\mu\text{m}$  diameter after 15 hours of polarization at  $-1400\text{ mV}$  and in situ testing. The surface integrity of the pillars were preserved perfectly using the glycerol-borax solution, and the activated slip systems after in situ deformation were visible. Fig. 13 shows the stress-strain curves of the compression tests. Load drops in the stress-strain curve are due to the plastic instabilities of material during displacement controlled tests. These load drops are the same as the strain bursts in the load controlled tests. There is a small change in the mechanical behavior of the pillars when compressed in air (EP) and in the presence of H (EP+C). Fe-3wt.% Si alloy has a BCC microstructure with a low H solubility but high H diffusivity. The diffusion coefficient of H in BCC iron was reported to be  $7 \times 10^{-5}\text{ cm}^2/\text{s}$  at room temperature [51, 59] and calculated to be  $\sim 4 \times 10^{-7}\text{ cm}^2/\text{s}$  in this study. H diffusion depth can be estimated by  $\sqrt{Dt}$ , where D is the diffusion coefficient and t is the H charging time. H can leave the interstitial places and diffuse out of the pillar radius ( $0.5\ \mu\text{m}$ ) under compression stress in  $3.45 \times 10^{-5}$  to  $6.25 \times 10^{-3}\text{ s}$ . Given that the compression tests were done under a displacement rate of  $1\text{ nm/s}$ , most of the H could be diffused out of the pillar during the first second of testing. Although the new electrolyte provides the possibility of preserving the integrity of the micron-sized samples during electrochemical testing, the small-scale compression testing is a challenging task to capture the H effect on the mechanical properties of the materials. The small-scale compression testing may be valid only for materials with low diffusivity under very high displacement rate.

310

315

320

[Figure 12 about here.]

[Figure 13 about here.]

### 3.4.3. *In situ electrochemical cantilever bending test*

In situ cantilever bending tests were done under cathodic current density (EP+C) and the results were compared with the bending condition in air (EP). The sample surface roughness alternation was negligible at the end of the in situ test. SEM images of the bent cantilevers after bending are shown in Fig. 14. While notch blunting occurred for the beams bent in air, H-assisted cracking is observed for all the beams bent in the presence of H. Comparing the load-displacement curves of the bending tests in air and under cathodic current density, there is a distinct influence of H on the mechanical properties of the Fe-3wt.%Si micro-cantilevers. Beams bent in air showed a continuous deformation after the yield point, with a slight hardening rate up to the final  $5\ \mu\text{m}$  displacement. While for H charged beams a gradual reduction in the flow curve after the yield point followed by a continuous rapid decrease in the load

325

330

from  $\sim 4 \mu\text{m}$  displacement. This rapid decrease of the load can be due to the crack propagation in the presence of H and decrease in the sample cross sectional area. H promotes the plasticity by lowering the activation energy for dislocation nucleation. Heterogeneous dislocation nucleation at the surface and reduction of double kink dislocation nucleation energy in the case of screw dislocations facilitates in the presence of H and promotes the plasticity. H-assisted cracking occurrence during in situ electrochemical cantilever bending test of the Fe-3wt% Si alloy in the presence of H with out any damage to the integrity of the micro-cantilever and preserving the surface roughness intact, indicates the capability if the glycerol-based solution toward small-scale HE testing.

[Figure 14 about here.]

#### 4. Conclusion

A novel electrolyte, with a composition of 1.3 mol/L borax in glycerol, diluted with double distilled water of 20 volume percent was introduced in this study. The electrolyte provides a unique capability to study HE at small scales such as nano- or micro-scale and can be considered as a suitable replacement for aqueous base solutions. Steady-state oxidation current density detection in the anodic side of the permeation cell, verified through permeation, electrochemical, surface chemical composition analyzes, and also in situ small-scale nanomechanical testing. Based on the results presented above, the following conclusions were drawn:

- Steady state permeation current was detected in the oxidation side of the cell, under different current densities and temperatures. This confirmed the formation and adsorption of H from the suggested glycerol-borax electrolyte.
- The surface analysis revealed minimal chemical alternation on the surface of samples after different electrochemical treatments. The iron oxide components of the sample with different electrochemical background followed a same trend in spite of small differences in their percentage. Thinner but denser oxide layer was detected for the anodically polarized sample in comparison to the other two samples.
- In situ electrochemical nano-indentation tests were done under cathodic potential and the L–D curves were compared with the results obtained under anodic polarization and after EP. Since the surface chemical composition and roughness were comparable in three different testing conditions, the observed changes in the pop-in load were considered as the subsurface H effect.
- The integrity of the micron-sized pillars and cantilevers was preserved at nano-scale using the new electrolyte.
- H-assisted cracking was observed for the cantilevers bent in situ under cathodic current density.

#### Acknowledgment

This research was supported by the Research Council of Norway through the HIPP project (Hydrogen-Induced Degradation of Offshore Steels in Aging Infrastructured Models for Prevention and Prediction) under project number

234130/E30 and HyF-Lex (244068/E30). The Research Council of Norway is acknowledged for their support of the NTNU NanoLab through the Norwegian Micro- and Nano-Fabrication Facility, Norfab (197411/V30). The authors thank Søren Heinze for his help with the DSC measurement.

## 365 References

- [1] Z. Zhang, G. Obasi, R. Morana, M. Preuss, Hydrogen assisted crack initiation and propagation in a nickel-based superalloy, *Acta Materialia* 113 (2016) 272–283, ISSN 1359-6454.
- [2] T. Depover, D. P. Escobar, E. Wallaert, Z. Zermout, K. Verbeken, Effect of hydrogen charging on the mechanical properties of advanced high strength steels, *International Journal of Hydrogen Energy* 39 (9) (2014) 4647–4656.
- 370 [3] I. M. Robertson, P. Sofronis, A. Nagao, M. Martin, S. Wang, D. Gross, K. Nygren, Hydrogen embrittlement understood, *Metall Mater Trans B* 46 (3) (2015) 1085–1103.
- [4] S. Frappart, X. Feaugas, J. Creus, F. Thebault, L. Delattre, H. Marchebois, Hydrogen solubility, diffusivity and trapping in a tempered FeCCr martensitic steel under various mechanical stress states, *Materials Science and Engineering: A* 534 (2012) 384–393, ISSN 0921-5093.
- [5] W. H. Johnson, On Some Remarkable Changes Produced in Iron and Steel by the Action of Hydrogen and Acids, *Proceedings of the Royal Society of London* 23 (156-163) (1874) 168–179.
- 375 [6] R. Oriani, The diffusion and trapping of hydrogen in steel, *Acta Metallurgica* 18 (1) (1970) 147 – 157, ISSN 0001-6160.
- [7] W. W. Gerberich, Y. Chen, Hydrogen-controlled cracking: An approach to threshold stress intensity, *Metallurgical and Materials Transactions A* 6 (2) (1975) 271–278.
- [8] H. Vehoff, W. Rothe, Gaseous hydrogen embrittlement in FeSi- and Ni-single crystals, *Acta Metall Mater* 31 (11) (1983) 1781–1793.
- 380 [9] S. Lynch, Environmentally assisted cracking: overview of evidence for an adsorption-induced localised-slip process, *Acta Metallurgica* 36 (10) (1988) 2639–2661.
- [10] P. Sofronis, H. Birnbaum, Mechanics of the hydrogen-dislocation-impurity interactions I. Increasing shear modulus, *Journal of the Mechanics and Physics of Solids* 43 (1) (1995) 49 – 90, ISSN 0022-5096.
- [11] R. Kirchheim, Revisiting hydrogen embrittlement models and hydrogen-induced homogeneous nucleation of dislocations, *Scripta Materialia* 62 (2) (2010) 67 – 70, ISSN 1359-6462.
- 385 [12] S. Wang, M. L. Martin, I. M. Robertson, P. Sofronis, Effect of hydrogen environment on the separation of Fe grain boundaries, *Acta Materialia* 107 (2016) 279 – 288, ISSN 1359-6454.
- [13] M. Koyama, H. Springer, S. V. Merzlikin, K. Tsuzaki, E. Akiyama, D. Raabe, Hydrogen embrittlement associated with strain localization in a precipitation-hardened Fe - Mn - Al - C light weight austenitic steel, *International Journal of Hydrogen Energy* 39 (9) (2014) 4634 – 4646, ISSN 0360-3199.
- 390 [14] M. Martin, B. Somerday, R. Ritchie, P. Sofronis, I. Robertson, Hydrogen-induced intergranular failure in nickel revisited, *Acta Materialia* 60 (6) (2012) 2739 – 2745, ISSN 1359-6454.
- [15] L. Marchetti, E. Herms, P. Laghoutaris, J. Chne, Hydrogen embrittlement susceptibility of tempered 9%Cr 1%Mo steel, *International Journal of Hydrogen Energy* 36 (24) (2011) 15880–15887, ISSN 0360-3199.
- 395 [16] G. Egels, L. Mujica Roncery, R. Fussik, W. Theisen, S. Weber, Impact of chemical inhomogeneities on local material properties and hydrogen environment embrittlement in AISI 304L steels, *International Journal of Hydrogen Energy* 43 (10) (2018) 5206–5216.
- [17] G. Stenerud, S. Wenner, J. S. Olsen, R. Johnsen, Effect of different microstructural features on the hydrogen embrittlement susceptibility of alloy 718, *International Journal of Hydrogen Energy* 43 (13) (2018) 6765–6776.
- [18] Y. Mine, N. Horita, Z. Horita, K. Takashima, Effect of ultrafine grain refinement on hydrogen embrittlement of metastable austenitic stainless steel, *International Journal of Hydrogen Energy* 42 (22) (2017) 15415–15425.
- 400 [19] W. L. Costin, O. Lavigne, A. Kotousov, R. Ghomashchi, V. Linton, Investigation of hydrogen assisted cracking in acicular ferrite using site-specific micro-fracture tests, *Materials Science and Engineering: A* 651 (2016) 859 – 868, ISSN 0921-5093.

- [20] D. Armstrong, M. Rogers, S. Roberts, Micromechanical testing of stress corrosion cracking of individual grain boundaries, *Scripta Mater* 61 (7) (2009) 741 – 743, ISSN 1359-6462.
- 405 [21] N. Kheradmand, A. F. Knorr, M. Marx, Y. Deng, Microscopic incompatibility controlling plastic deformation of bicrystals, *Acta Materialia* 106 (2016) 219–228, ISSN 1359-6454.
- [22] K. Nibur, D. Bahr, B. Somerday, Hydrogen effects on dislocation activity in austenitic stainless steel, *Acta Mater.* 54 (10) (2006) 2677–2684, ISSN 13596454.
- [23] E. Tal-Gutelmacher, R. Gemma, C. Volkert, R. Kirchheim, Hydrogen effect on dislocation nucleation in a vanadium (1 0 0) single crystal as  
410 observed during nanoindentation, *Scripta Mater* 63 (10) (2010) 1032 – 1035, ISSN 1359-6462.
- [24] J. Wheeler, T. Clyne, Nanoindentation of palladium–hydrogen, *International Journal of Hydrogen Energy* 37 (19) (2012) 14315–14322.
- [25] B. R. S. Rogne, N. Kheradmand, Y. Deng, A. Barnoush, In situ micromechanical testing in environmental scanning electron microscope: A new insight into hydrogen-assisted cracking, *Acta Materialia* ISSN 1359-6454.
- [26] Y. Deng, A. Barnoush, Hydrogen embrittlement revealed via novel in situ fracture experiments using notched micro-cantilever specimens,  
415 *Acta Materialia* 142 (Supplement C) (2018) 236–247, ISSN 1359-6454.
- [27] Y. He, Y. Li, C. Chen, H. Yu, Diffusion coefficient of hydrogen interstitial atom in  $\alpha$ -Fe,  $\gamma$ -Fe and  $\epsilon$ -Fe crystals by first-principle calculations, *International Journal of Hydrogen Energy* ISSN 0360-3199.
- [28] S. L. E. Akiyama, Electrochemical Hydrogen Permeation Tests under Conventional Potentiostatic Hydrogen Charging Conditions for Hydrogen Embrittlement Study, *ECS Transactions* 75 (2017) 23–31.
- 420 [29] M. Kappes, G. Frankel, R. Thodla, M. Mueller, N. Sridhar, R. Carranza, Hydrogen Permeation and Corrosion Fatigue Crack Growth Rates of X65 Pipeline Steel Exposed to Acid Brines Containing Thiosulfate or Hydrogen Sulfide, *Corrosion* 68 (11) (2012) 1015–1028.
- [30] I. Gutierrez-Urrutia, S. Zaeferrer, D. Raabe, Electron channeling contrast imaging of twins and dislocations in twinning-induced plasticity steels under controlled diffraction conditions in a scanning electron microscope, *Scripta Materialia* 61 (7) (2009) 737–740, ISSN 1359-6462.
- [31] O. Sobol, G. Nolze, R. Saliwan-Neumann, D. Eliezer, T. Böellinghaus, W. E. S. Unger, Novel approach to image hydrogen distribution and related phase transformation in duplex stainless steels at the sub-micron scale, *International Journal of Hydrogen Energy* 42 (39) (2017) 25114–25120.  
425
- [32] A. Kocijan, r. Donik, M. Jenko, Electrochemical and XPS studies of the passive film formed on stainless steels in borate buffer and chloride solutions, *Corrosion Science* 49 (5) (2007) 2083–2098, ISSN 0010-938X.
- [33] J. M. Macak, H. Tsuchiya, L. Taveira, S. Aldabergerova, P. Schmuki, Smooth anodic TiO<sub>2</sub> nanotubes, *Angewandte Chemie International Edition* 44 (45) (2005) 7463–7465.  
430
- [34] J. M. Macak, P. Schmuki, Anodic growth of self-organized anodic TiO<sub>2</sub> nanotubes in viscous electrolytes, *Electrochimica Acta* 52 (3) (2006) 1258–1264.
- [35] R. V. Devireddy, P. H. Leo, J. S. Lowengrub, J. C. Bischof, Measurement and numerical analysis of freezing in solutions enclosed in a small container, *International Journal of Heat and Mass Transfer* 45 (9) (2002) 1915–1931.
- 435 [36] I. Bernstein, G. Pressouyre, R. Oriani, J. Hirth, Hydrogen Degradation of Ferrous Alloys, Noyes Publ., Park Ridge, USA (1985) 641.
- [37] F. Matjaž, J. Jackson, Application of corrosion inhibitors for steels in acidic media for the oil and gas industry: A review, *Corrosion Science* 86 (2014) 17–41, ISSN 0010-938X.
- [38] Y. Takahashi, K. Yamaguchi, M. Tanaka, K. Higashida, H. Noguchi, On the micromechanism of hydrogen-assisted cracking in a single-crystalline iron-silicon alloy thin sheet, *Scripta Materialia* 64 (6) (2011) 537 – 540, ISSN 1359-6462.
- 440 [39] Standard Practice for Evaluation of Hydrogen Uptake, Permeation, and Transport in Metals by an Electrochemical Technique, 2011.
- [40] A. Barnoush, H. Vehoff, Recent developments in the study of hydrogen embrittlement: Hydrogen effect on dislocation nucleation, *Acta Mater* 58 (16) (2010) 5274 – 5285, ISSN 1359-6454.
- [41] D. A. Shirley, High-Resolution X-Ray Photoemission Spectrum of the Valence Bands of Gold, *Phys. Rev. B* 5 (1972) 4709–4714.
- [42] C. Schmidt, H.-H. Strehlow, XPS investigations on the formation of passive layers on Fe/Si alloys at pH 5 and 9, *Surface and interface analysis* 27 (11) (1999) 984–992.  
445

- [43] W. Fredriksson, S. Malmgren, T. Gustafsson, M. Gorgoi, K. Edström, Full depth profile of passive films on 316L stainless steel based on high resolution HAXPES in combination with ARXPS, *Applied Surface Science* 258 (15) (2012) 5790 – 5797, ISSN 0169-4332.
- [44] A. Barnoush, J. Dake, N. Kheradmand, H. Vehoff, Examination of hydrogen embrittlement in FeAl by means of in situ electrochemical micropillar compression and nanoindentation techniques, *Intermetallics* 18 (7) (2010) 1385–1389, ISSN 0966-9795.
- 450 [45] T. Hajilou, Y. Deng, B. R. Rogne, N. Kheradmand, A. Barnoush, In situ electrochemical microcantilever bending test: A new insight into hydrogen enhanced cracking, *Scripta Materialia* 132 (2017) 17 – 21, ISSN 1359-6462.
- [46] L. A. Toledo-Matos, M. A. Pech-Canul, Evolution of an iron passive film in a borate buffer solution (pH=8.4), *Journal of Solid State Electrochemistry* 15 (9) (2011) 1927–1934, ISSN 1433-0768.
- [47] D. P. Escobar, C. Miambres, L. Duprez, K. Verbeken, M. Verhaege, Internal and surface damage of multiphase steels and pure iron after electrochemical hydrogen charging, *Corrosion Science* 53 (10) (2011) 3166 – 3176, ISSN 0010-938X.
- 455 [48] M. Warrior, A. Rai, R. Schneider, A time dependent model to study the effect of surface roughness on reactive-diffusive transport in porous media, *Journal of Nuclear Materials* 390 (2009) 203 – 206, ISSN 0022-3115, proceedings of the 18th International Conference on Plasma-Surface Interactions in Controlled Fusion Device.
- [49] D. Pérez Escobar, K. Verbeken, L. Duprez, M. Verhaege, On the methodology of Thermal Desorption Spectroscopy to evaluate hydrogen embrittlement, in: *Materials Science Forum*, vol. 706, Trans Tech Publ, 2354–2359, 2012.
- 460 [50] H. Husby, M. Iannuzzi, R. Johnsen, M. Kappes, A. Barnoush, Effect of nickel on hydrogen permeation in ferritic/pearlitic low alloy steels, *International Journal of Hydrogen Energy* 43 (7) (2018) 3845–3861, ISSN 0360-3199.
- [51] H. Hagi, Y. Hayashi, N. Ohtani, Diffusion Coefficient of Hydrogen in Pure Iron between 230 and 300 K, *Transactions of the Japan Institute of Metals* 20 (7) (1979) 349–357.
- 465 [52] I. M. Bernstein, The role of hydrogen in the embrittlement of iron and steel, *Materials Science and Engineering* 6 (1) (1970) 1–19, ISSN 0025-5416.
- [53] V. I. Saliy, R. A. Ryabov, P. V. Gel'd, Coefficients of hydrogen diffusion and solubility in solid solutions of silicon in iron, *Physics of Metals and Metallography* 35 (1) (1973) 106–110.
- [54] A. H. Zavieh, N. Espallargas, The role of surface chemistry and fatigue on tribocorrosion of austenitic stainless steel, *Tribology International* 103 (2016) 368–378, ISSN 0301-679X.
- 470 [55] S. Modiano, J. Carreo, C. Fugivara, R. Torresi, V. Vivier, A. Benedetti, O. Mattos, Changes on iron electrode surface during hydrogen permeation in borate buffer solution, *Electrochimica Acta* 53 (10) (2008) 3670 – 3679, ISSN 0013-4686.
- [56] A. Barnoush, M. Asgari, R. Johnsen, Resolving the hydrogen effect on dislocation nucleation and mobility by electrochemical nanoindentation, *Scr. Mater.* 66 (6) (2012) 414–417, ISSN 13596462.
- 475 [57] A. Barnoush, H. Vehoff, In situ electrochemical nanoindentation of a nickel (111) single crystal: Hydrogen effect on pop-in behaviour, *Zeitschrift für Metallkunde* 97 (9) (2006) 1224–1229, ISSN 0044-3093.
- [58] A. Barnoush, C. Bies, H. Vehoff, In situ electrochemical nanoindentation of FeAl (100) single crystal: Hydrogen effect on dislocation nucleation, *Journal of Materials Research* 24 (03) (2009) 1105–1113, ISSN 2044-5326.
- [59] K. Kiuchi, R. B. McLellan, The solubility and diffusivity of hydrogen in well-annealed and deformed iron, *Acta Metallurgica* 31 (7) (1983) 961–984, ISSN 0001-6160.
- 480

**List of Tables**

1	Composition of Fe–3wt.%Si alloy used in this study . . . . .	17
2	Peak position and curve fit parameters of iron and silicon of XPS analysis . . . . .	18
3	Effective diffusion coefficient, $D_{\text{eff}}$ , and subsurface hydrogen concentration, $C_0$ , results for Fe–3wt.%Si calculated by $t_{\text{lag}}$ method. . . . .	19



Table 1: Composition of Fe-3wt.%Si alloy used in this study

Element	C	Si	Mn	P	S	Cr	Ni	Mo	Cu	Al	Ti	Nb	V	B	Zr	Ce
Weight%	0.003	2.383	0.202	0.013	0.012	0.033	0.048	0.015	0.020	0.365	0.005	0.020	0.002	0.0008	0.005	0.009

Table 2: Peak position and curve fit parameters of iron and silicon of XPS analysis

Peak	$Fe2p_{3/2}$	$FeO$	$Fe_3O_4$	$Fe^{3+}$	$Si2p$	$Si^{4+}$	$O^{2-}$ in $Fe_2O_3$	$O^{2-}$ in $Fe_2SiO_4$	$OH^-$	$O^{2-}$ in $SiO_2$
B.E%	706.72	+2.6	+4.1	+5.9	530.2	+1.5	543.5	+0.7	+1.85	+2.3
FWHM	0.9	2	2	1.85	0.85	1.3	1	1	1.5	2.5
Line shape	L.A(1.2.5.1)	GL(0)	GL(0)	GL(0)	GL(30)	GL(30)	GL(30)	GL(30)	GL(30)	GL(30)

Table 3: Effective diffusion coefficient,  $D_{\text{eff}}$ , and subsurface hydrogen concentration,  $C_0$ , results for Fe-3wt.%Si calculated by  $t_{\text{lag}}$  method.

Trans. No., Temp.	$i_c(\mu\text{A}/\text{cm}^{-2})$	$t_{\text{lag}}(\text{s})$	$i_{\text{ss}}(\mu\text{A}/\text{cm}^{-2})$	$D_{\text{eff}}(\text{cm}^2\text{s}^{-1})$	$C_0(\text{wppm})$
1, 50 °C	-100	2232	$1.43 \times 10^{-1}$	$6.633 \times 10^{-7}$	$2.69 \times 10^{-2}$
2, 50 °C	-100	4257	$1.54 \times 10^{-1}$	$3.478 \times 10^{-7}$	$5.54 \times 10^{-2}$
3, 50 °C	-100	4545	$1.32 \times 10^{-1}$	$3.257 \times 10^{-7}$	$5.05 \times 10^{-2}$
1, 50 °C	-50	2949	$1.72 \times 10^{-1}$	$5.020 \times 10^{-7}$	$4.31 \times 10^{-2}$
2, 50 °C	-50	2532	$1.36 \times 10^{-1}$	$5.847 \times 10^{-7}$	$2.93 \times 10^{-2}$
3, 50 °C	-50	2529	$1.55 \times 10^{-1}$	$5.854 \times 10^{-7}$	$3.31 \times 10^{-2}$
1, 50 °C	-10	3138	$3.63 \times 10^{-2}$	$4.718 \times 10^{-7}$	$1.02 \times 10^{-2}$
2, 50 °C	-10	3594	$3.40 \times 10^{-2}$	$4.119 \times 10^{-7}$	$1.03 \times 10^{-2}$
3, 50 °C	-10	4542	$3.40 \times 10^{-2}$	$3.260 \times 10^{-7}$	$1.26 \times 10^{-2}$
1, 30 °C	-10	7065	$1.14 \times 10^{-2}$	$2.096 \times 10^{-7}$	$6.33 \times 10^{-3}$
1, 30 °C	-10	5931	$9.09 \times 10^{-3}$	$2.496 \times 10^{-7}$	$4.23 \times 10^{-3}$
1, 30 °C	-10	6546	$9.09 \times 10^{-3}$	$2.262 \times 10^{-7}$	$4.77 \times 10^{-3}$

**List of Figures**

	1	Scanning electron microscopic image of the Fe–3wt.% Si, micro-pillars after in situ electrochemical pillar compression test inside an aqueous borate-buffer solution. . . . .	21
490	2	: The differential scanning calorimetry measured thermogram of the glycerol-borax solution obtained at 10 °C/min scan rate measurements. . . . .	22
	3	Schematic representation of the in situ electrochemical three-electrode cell used for micro-pillar compression and cantilever bending tests under cathodic potentials. . . . .	23
	4	Secondary electron images of the Fe–3wt% Si (a) micro-pillar and (b) micro-cantilever. . . . .	24
495	5	Polarization curve of Fe–3wt.%Si in glycerol-borax solution at a scan rate of 1 mV/s at room temperature. . . . .	25
	6	Permeation transients of Fe–3wt.%Si sample under different current densities plotted as steady-state normalized permeation flux vs. the logarithm of normalized time. . . . .	26
	7	Atomic concentration of different elements versus sputtering time at three different testing conditions. . . . .	27
	8	Comparing the iron oxide components in three different testing conditions. . . . .	28
500	9	Atomic ratio of O/Fe at surface of three different testing samples versus sputtering time. . . . .	29
	10	Comparing the iron and iron oxide peaks in three different testing conditions after 230 and 3000 seconds sputtering time. . . . .	30
505	11	a)Load–displacement curves, b)cumulative frequency distribution of pop-in load start and c)scanning probe microscopic images of in situ electrochemical nano-indentation testing in three different testing conditions. . . . .	31
	12	Secondary electron images of the micro-pillars after in situ pillar compression test inside the glycerol-borax solution. . . . .	32
	13	Stress–strain curves of pillars compressed in air and under cathodic potential of –1400 mV vs. Hg/HgSO <sub>4</sub> reference electrode, inside the glycerol-based solution. . . . .	33
510	14	a)Load-displacement curves of a micro-cantilevers bent in air and in the presence of H inside new glycerol-borax solution. Secondary electron images of the beam bent in the presence of H (b) and in air (c). Secondary electron image of the notch area for beams bent in the presence of H ( <i>b</i> <sub>1</sub> ) and in air ( <i>c</i> <sub>1</sub> ). . . . .	34

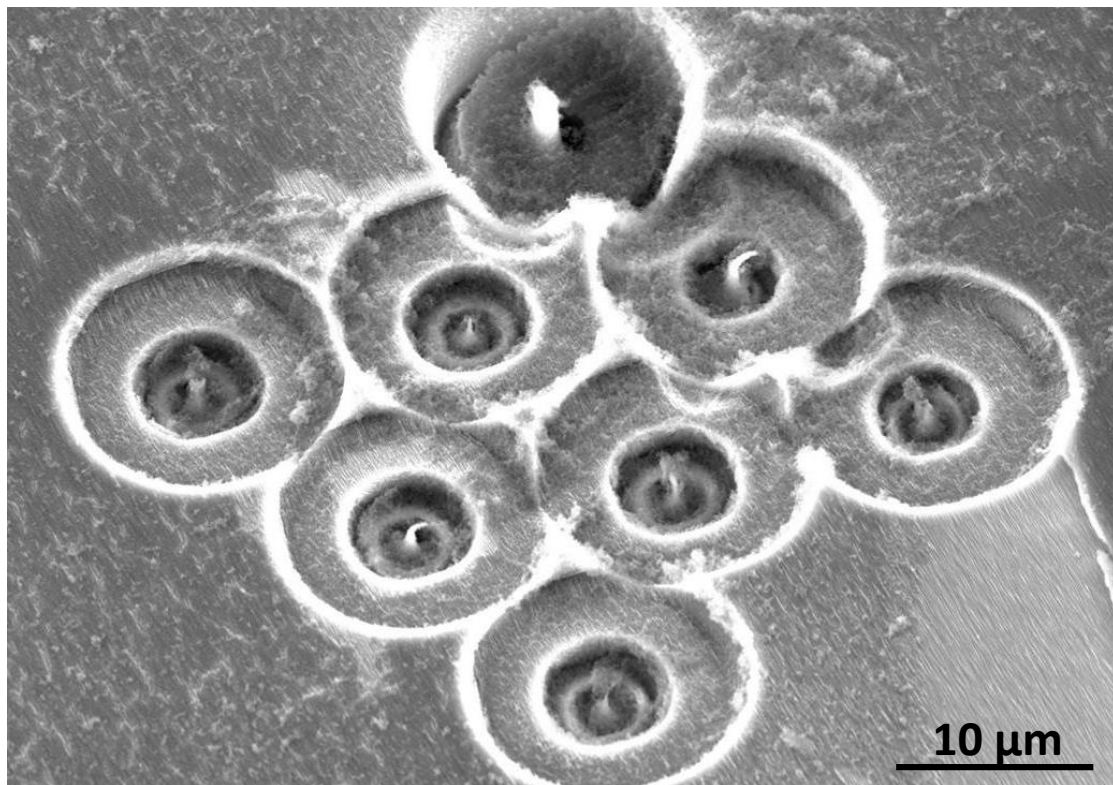


Figure 1: Scanning electron microscopic image of the Fe-3wt.% Si, micro-pillars after in situ electrochemical pillar compression test inside an aqueous borate-buffer solution.

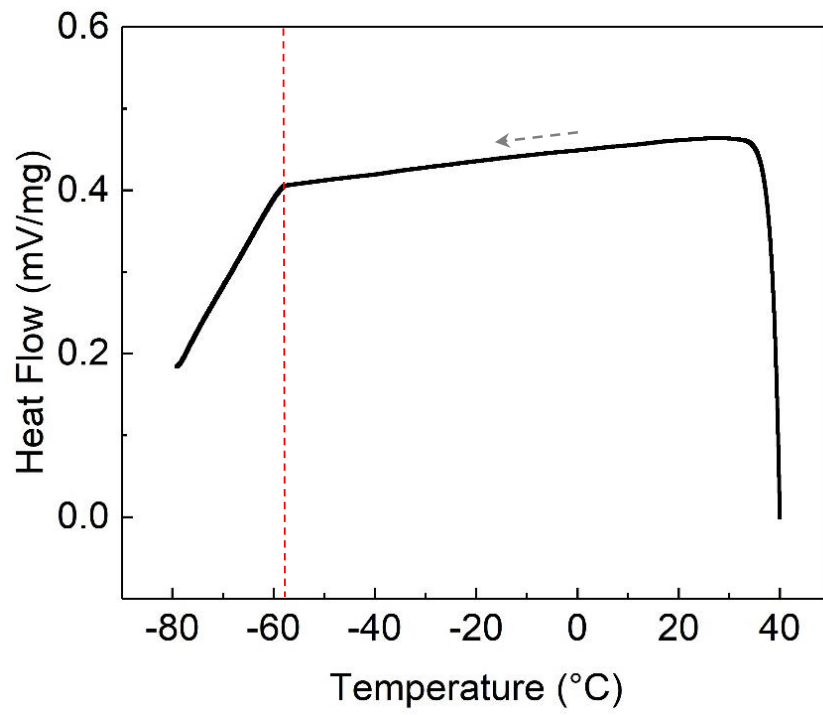


Figure 2: : The differential scanning calorimetry measured thermogram of the glycerol-borax solution obtained at 10 °C/min scan rate measurements.

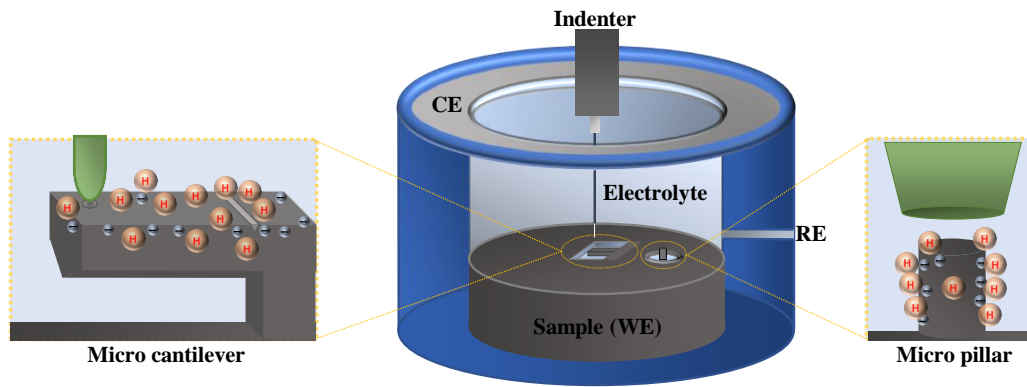


Figure 3: Schematic representation of the in situ electrochemical three-electrode cell used for micro-pillar compression and cantilever bending tests under cathodic potentials.

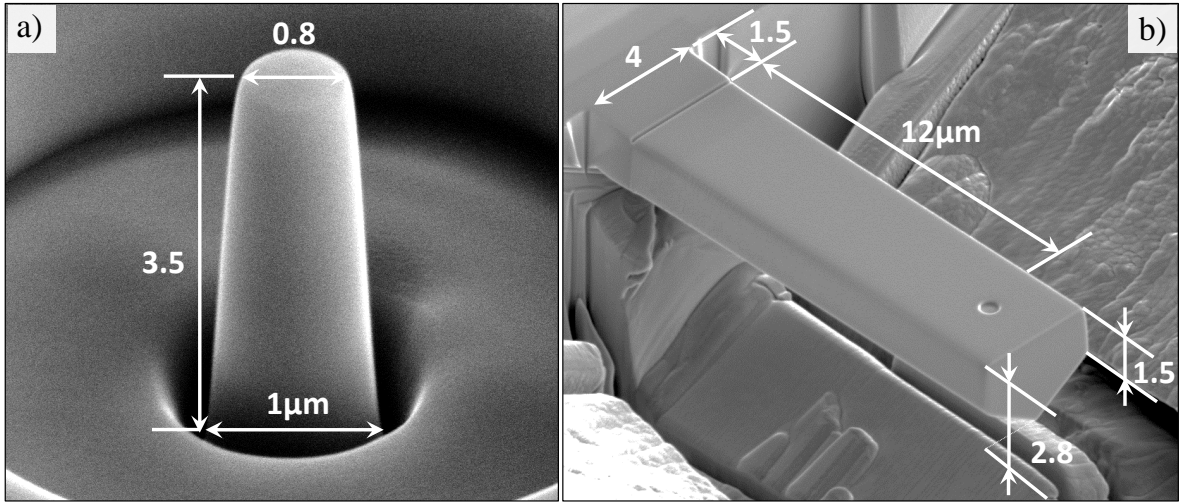


Figure 4: Secondary electron images of the Fe-3wt% Si (a) micro-pillar and (b) micro-cantilever.



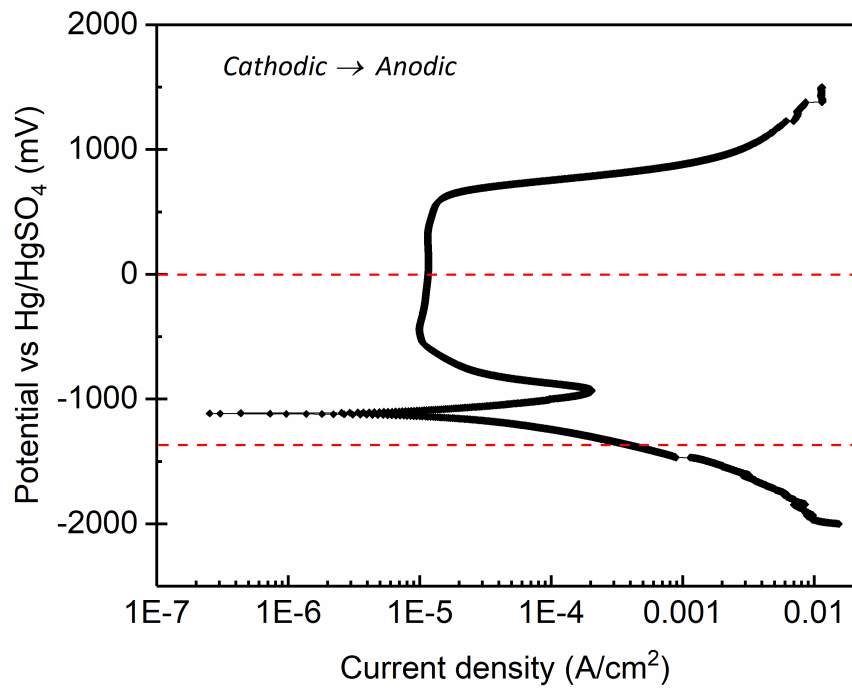


Figure 5: Polarization curve of Fe-3wt.%Si in glycerol-borax solution at a scan rate of 1 mV/s at room temperature.

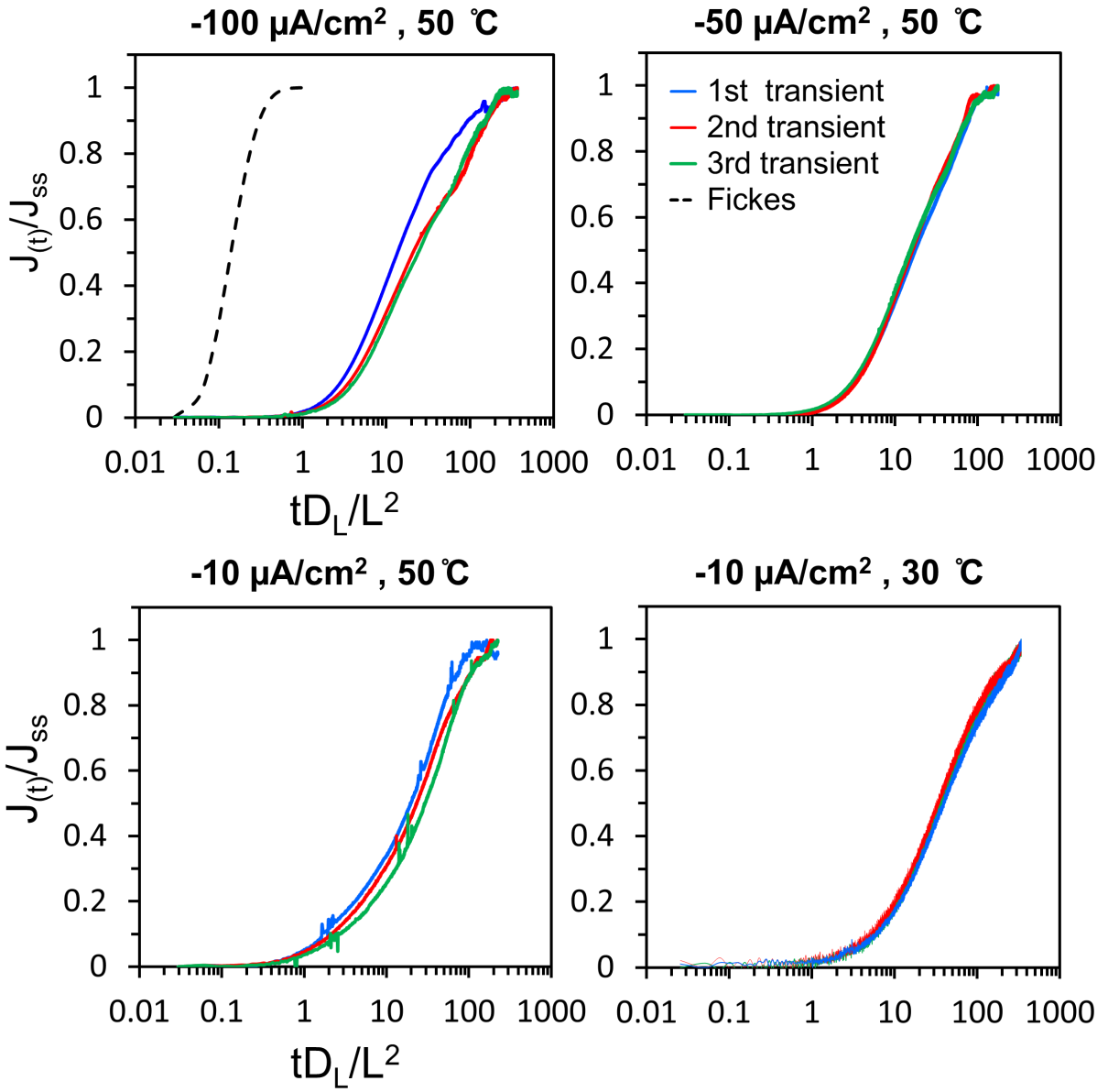


Figure 6: Permeation transients of Fe-3wt.%Si sample under different current densities plotted as steady-state normalized permeation flux vs. the logarithm of normalized time.

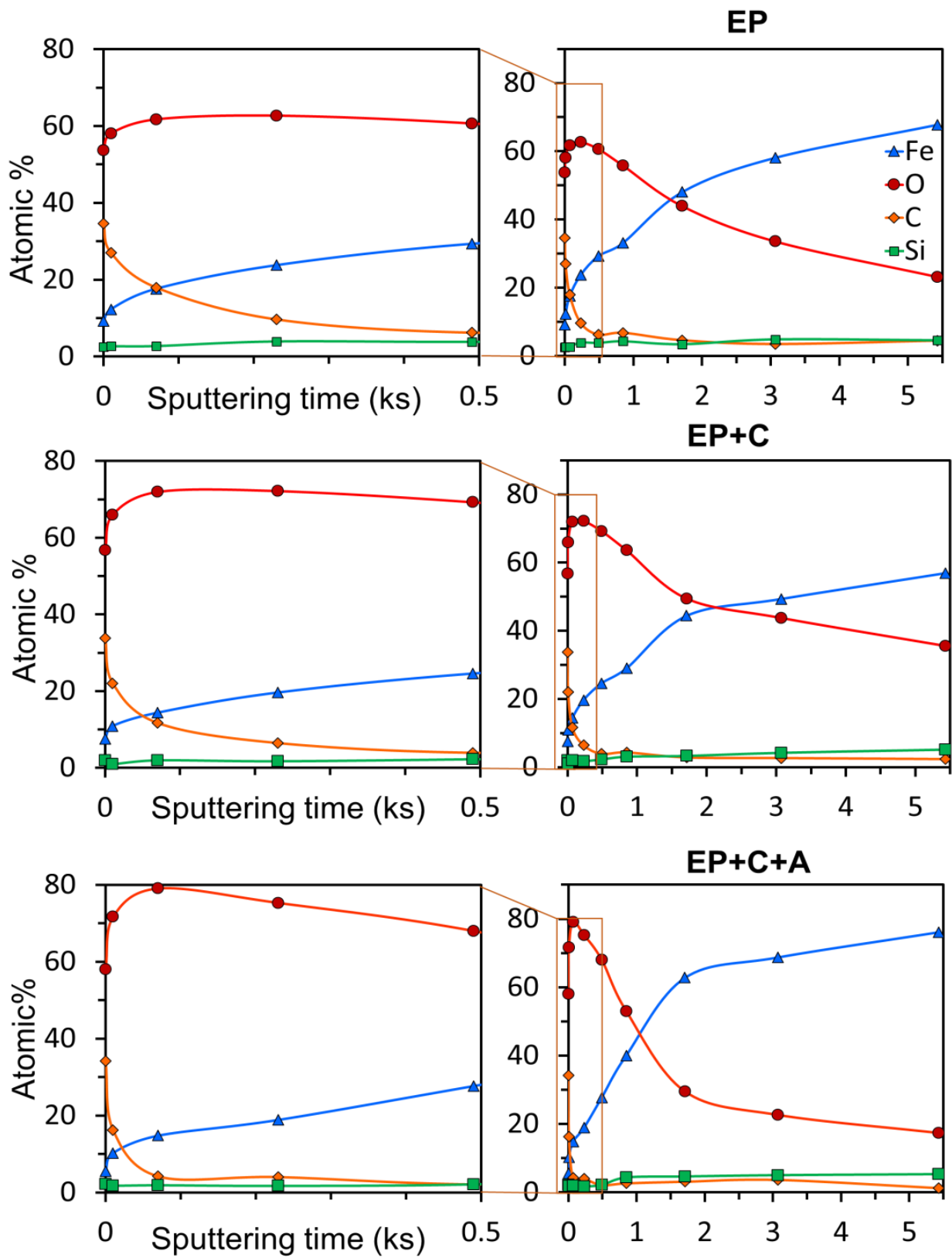


Figure 7: Atomic concentration of different elements versus sputtering time at three different testing conditions.

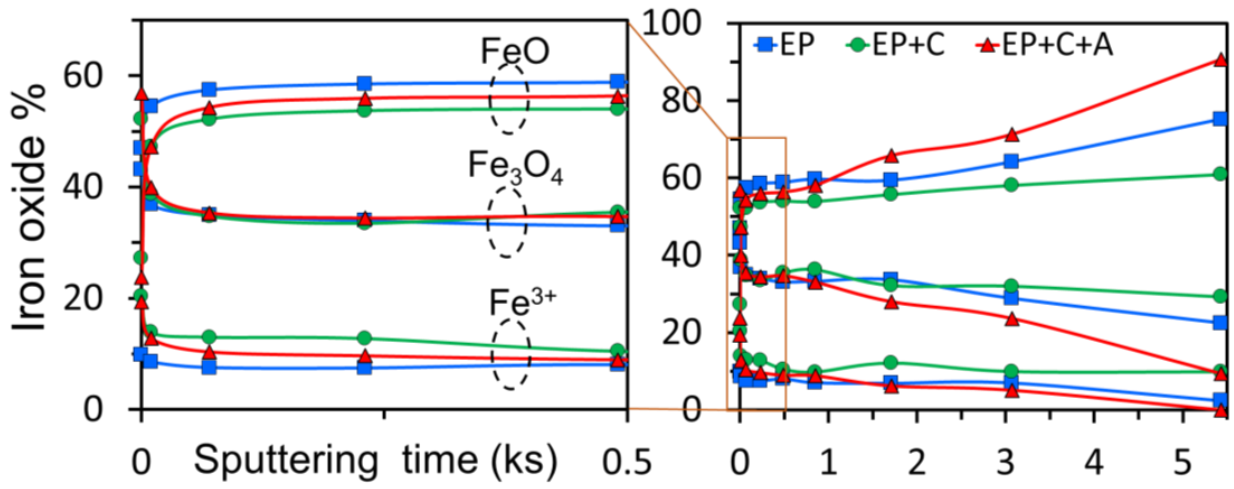


Figure 8: Comparing the iron oxide components in three different testing conditions.

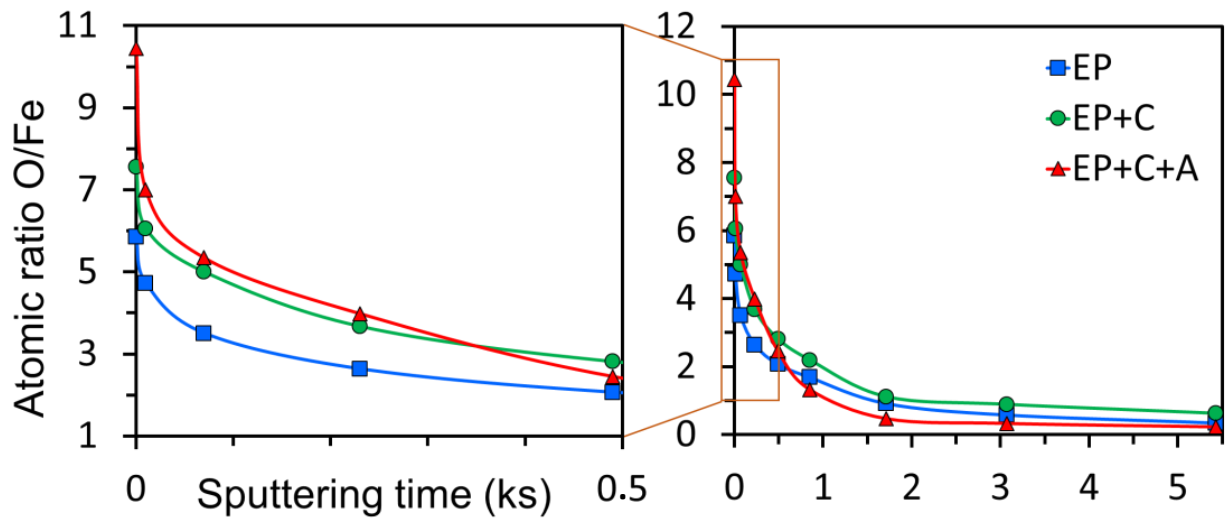


Figure 9: Atomic ratio of O/Fe at surface of three different testing samples versus sputtering time.

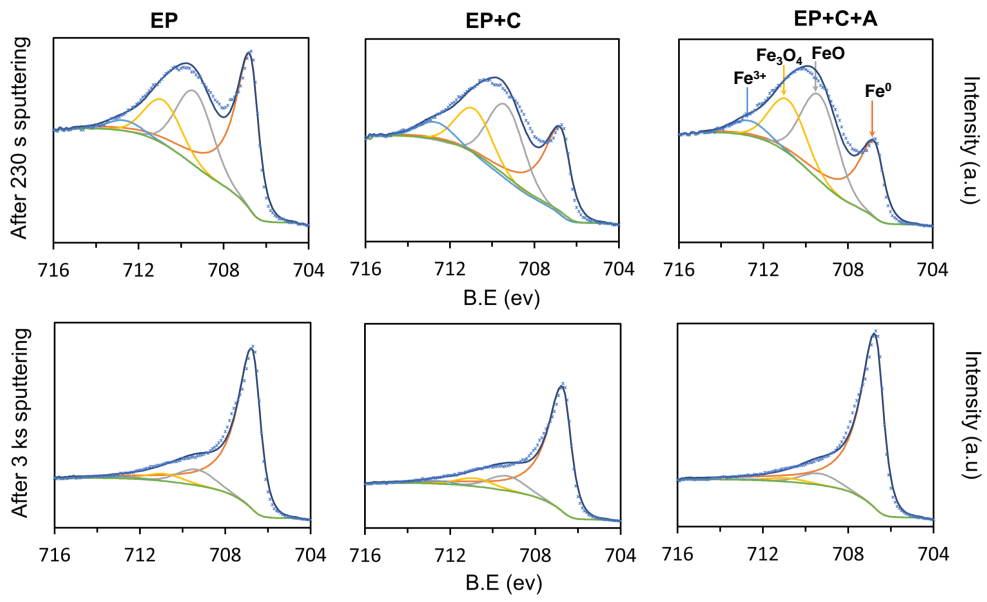


Figure 10: Comparing the iron and iron oxide peaks in three different testing conditions after 230 and 3000 seconds sputtering time.

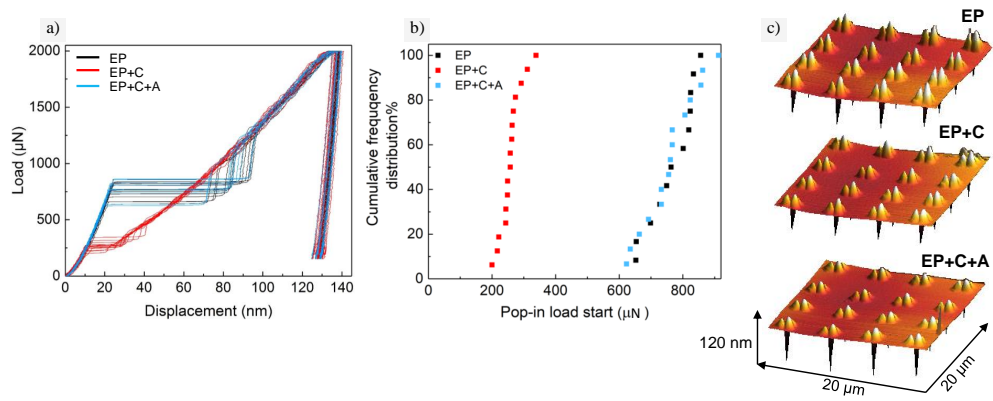


Figure 11: a) Load-displacement curves, b) cumulative frequency distribution of pop-in load start and c) scanning probe microscopic images of in situ electrochemical nano-indentation testing in three different testing conditions.

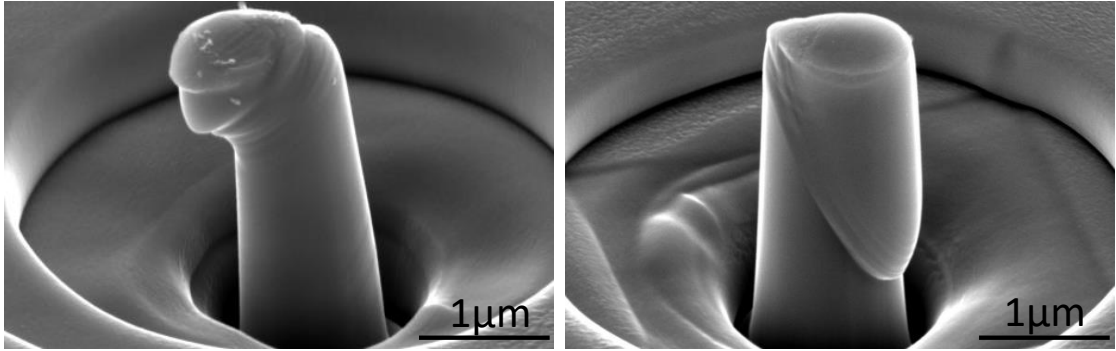


Figure 12: Secondary electron images of the micro-pillars after in situ pillar compression test inside the glycerol-borax solution.



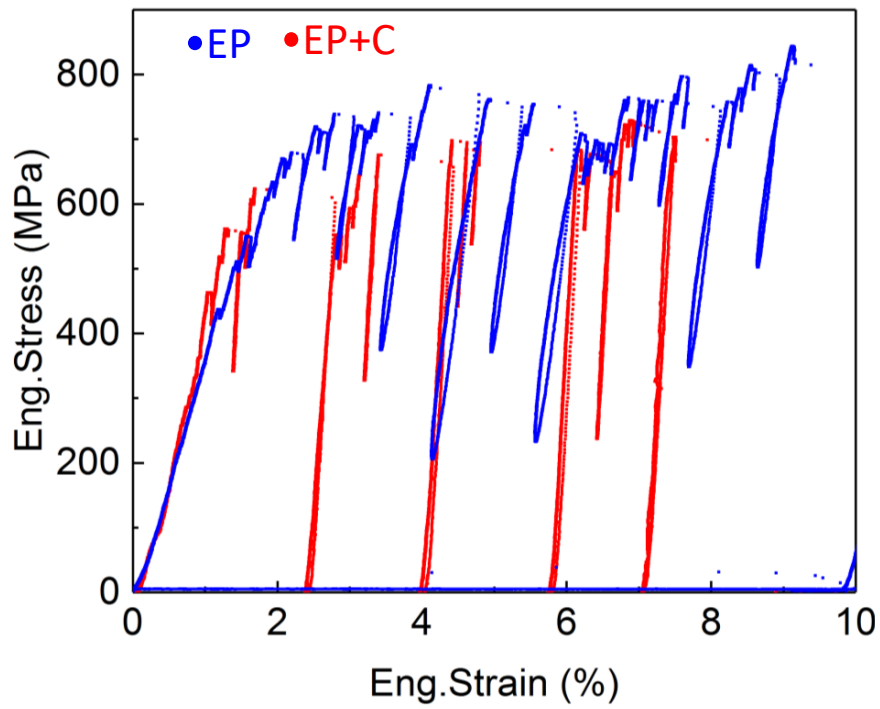


Figure 13: Stress–strain curves of pillars compressed in air and under cathodic potential of  $-1400$  mV vs. Hg/HgSO<sub>4</sub> reference electrode, inside the glycerol-based solution.

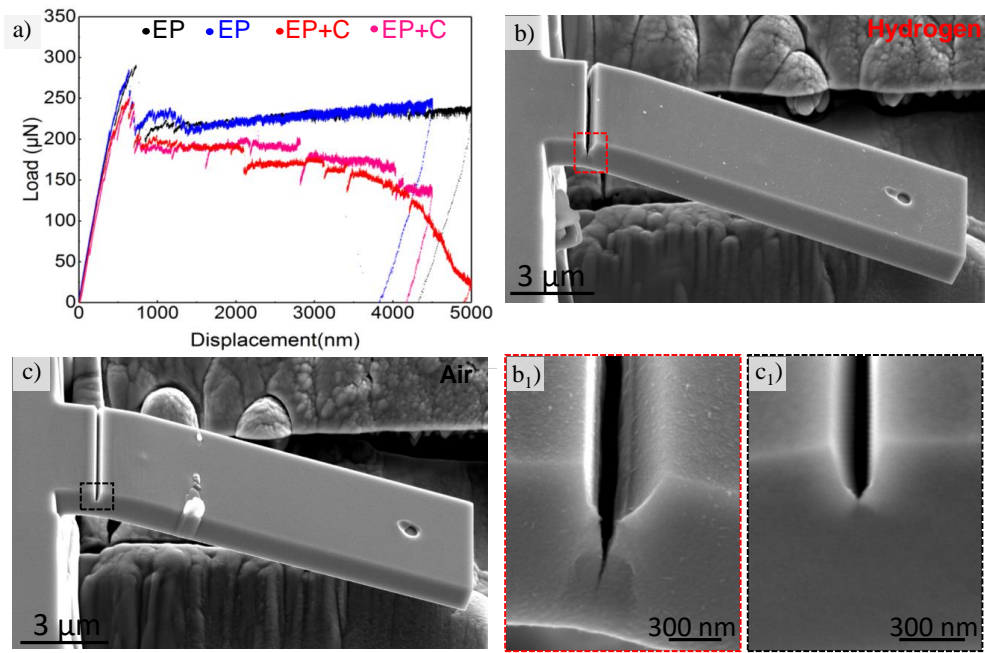


Figure 14: a) Load-displacement curves of a micro-cantilevers bent in air and in the presence of H inside new glycerol-borax solution. Secondary electron images of the beam bent in the presence of H (b) and in air (c). Secondary electron image of the notch area for beams bent in the presence of H ( $b_1$ ) and in air ( $c_1$ ).